Elastic scattering of protons from ^{9}C with a 290 MeV/nucleon ^{9}C beam

Y. Matsuda,[1,*] H. Sakaguchi,[2,†] H. Takeda,[3] S. Terashima,[3,‡] J. Zenihiro,[4,§] T. Kobayashi,[1] T. Murakami,[4] Y. Iwao,[4] T. Ichihara,[3] T. Suda,[3,‖] T. Ohnishi,[3] Y. Watanabe,[3] H. Otsu,[3] K. Yoneda,[3] Y. Satou,[5,¶] K. Ozeki,[6,§] and M. Kanazawa[7,**]

[1]*Department of Physics, Tohoku University, Miyagi 980-8578, Japan*
[2]*Department of Applied Physics, University of Miyazaki, Miyazaki 889-2192, Japan*
[3]*RIKEN Nishina Center for Accelerator-Based Science, RIKEN, Saitama 351-0198, Japan*
[4]*Department of Physics, Kyoto University, Kyoto 606-8502, Japan*
[5]*Department of Physics, Tokyo Institute of Technology, Tokyo 152-8551, Japan*
[6]*Cyclotron and Radioisotope Center, Tohoku University, Miyagi 980-8578, Japan*
[7]*National Institute of Radiological Sciences, Chiba 263-8555, Japan*

(Received 5 November 2012; published 12 March 2013)

The angular distribution of proton-^{9}C elastic scattering at 277–300 MeV/nucleon was measured with a newly designed recoil proton spectrometer. The angular distribution was analyzed using the relativistic impulse approximation. The root-mean-square matter radius of ^{9}C was deduced to be $2.43^{+0.55}_{-0.28}$ fm with different two-parameter Fermi density distributions for protons and neutrons.

DOI: 10.1103/PhysRevC.87.034614 PACS number(s): 25.60.Bx, 25.40.Cm, 24.10.Jv

I. INTRODUCTION

Recent progress in the study of unstable nuclei has triggered renewed interest in nuclear radii and proton and neutron density distributions [1,2], and proton elastic scattering at intermediate energies is one method of studying these distributions. Using a relativistic impulse approximation (RIA) or a folding model with complex g-matrix interaction, we can directly compare proton elastic scattering with nuclear density distributions.

For stable nuclei, the proton density distribution can be obtained by unfolding the charge distribution determined using electron scattering. A technique such as proton elastic scattering can then be used to deduce the neutron density distribution. In order to accomplish this, the angular distribution must be precisely reproduced. We thus introduced density-dependent phenomenological medium-effect parameters to scattering amplitudes used in an RIA [3] and tuned the scattering amplitudes with scattering data for a nucleus whose proton and neutron densities are thought to be the same shape and can be well inferred from the electron scattering [4,5].

For unstable nuclei, we do not have information from electron scattering. Thus we need to infer both proton and neutron density distributions from proton elastic scattering. We also need to tune the scattering amplitudes with scattering for a nearby stable $N = Z$ nucleus.

The matter and charge radii of various unstable nuclei have been deduced by measuring the interaction (reaction) cross sections and optical isotope shifts (see, e.g., [6,7]). However, the experiments performed at GSI are the only instance to date of proton elastic scattering for unstable nuclei at intermediate energies [8–10]. At 700 MeV/nucleon, experimenters at GSI have measured neutron-rich isotopes from helium to beryllium at the small angle region where the Glauber multiple-scattering theory is appropriate. These studies have examined the tail structure of the density distributions, comparing them with experimental data.

At 300 MeV, where nucleons have the longest mean free path in the nucleus, no quantitative or qualitative studies of proton elastic scattering for unstable nuclei have been made. We have therefore planned elastic scattering of protons with radioactive ion beams (ESPRI) and have constructed a recoil proton spectrometer (RPS). This work is devoted to reporting the first results using the RPS.

As the first measurement, we have measured the elastic scattering of protons from ^{9}C. It is believed that ^{9}C has a proton skin and a large matter radius due to the large difference between the proton and neutron numbers. In fact, these quantities may relate to the puzzle of the large isoscalar spin expectation value deduced from the magnetic moment [11,12]. Recently, Utsuno suggested that the shell quenching in ^{9}C accounts for the anomalous magnetic moment and breaks the mirror symmetry in the ground-state wave functions [13]. Therefore, ^{9}C is an interesting nucleus among carbon isotopes. In addition, this isotope located at the proton drip line has no bound excited states below the one- and two-proton separation energies. Hence, we have been able to identify the elastic events robustly as described in the next section.

The main purposes of this work are the application of our previous work [3–5] to the measurement of the unstable ^{9}C nucleus and deducing the matter radius. In this article, the

*Present address: Department of Physics, Kyoto University, Kyoto 606-8502, Japan; matsu@scphys.kyoto-u.ac.jp.
†Present address: Research Center for Nuclear Physics, Osaka University, Osaka 567-0047, Japan.
‡Present address: School of Physics and Nuclear Energy Engineering, Beihang University, Beijing 100191, China.
§Present address: RIKEN Nishina Center for Accelerator-Based Science, RIKEN, Saitama 351-0198, Japan.
‖Present address: Research Center for Electron Photon Science, Tohoku University, Miyagi 982-0826, Japan.
¶Present address: Department of Physics and Astronomy, Seoul National University, Seoul 151-742, Korea.
**Present address: Ion Beam Therapy Center, SAGA HIMAT Foundation, Saga 841-0071, Japan.

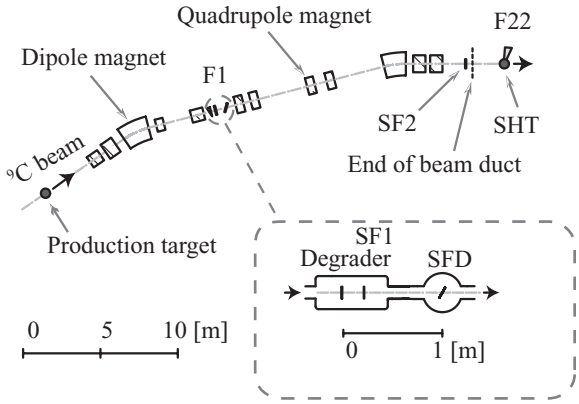

FIG. 1. Schematic view of the fragment separator in the HIMAC of the NIRS. The inset shows the experimental setup at the momentum-dispersive focal plane F1.

experimental results are reported in Sec. II and the matter radius is investigated in Sec. III. Finally, Sec. IV summarizes this study.

II. EXPERIMENT

A. Experimental setup

The experiment was performed at a secondary beam course (fragment separator) in the Heavy Ion Medical Accelerator in Chiba (HIMAC) of the National Institute of Radiological Science (NIRS) [14]. Figure 1 shows a schematic view of the fragment separator and the experimental setup at a momentum-dispersive focal plane F1. Figure 2 shows a schematic view of the experimental setup at an achromatic focal plane F22.

A ^{12}C beam was accelerated up to 430 MeV/nucleon with a heavy-ion synchrotron. The intensity was 6×10^9 particles per pulse; the repetition cycle and the duty factor of the pulse were 1/3.3 Hz and about 50%, respectively. A ^{9}C beam was produced by projectile fragmentation of the ^{12}C beam on a ^{9}Be target of 50 mm thickness. The ^{9}C beam was roughly distinguished from the cocktail beam using the fragment separator. The intensity of the secondary beam on a hydrogen target was 4×10^4 particles per pulse.

The ^{9}C beam was clearly selected from correlation between the energy loss in a 3-mm-thick plastic scintillator (SF3) and the time of flight (TOF) from a scintillating fiber detector (SFD) [15] to SF3. The SFD and SF3 were placed at the momentum-dispersive focal plane and behind an exit duct of the beam line, respectively. The SFD was tilted at an angle of 60° relative to the beam axis so that inefficient regions between fibers disappeared. From Ref. [15], the time and position resolutions of the SFD are estimated to be about 1 ns and less than 0.7 mm (root mean square, rms), respectively. We also used the SFD to tag the momentum of the beam by approximating the momentum to a simple function of the detected position. The function was determined by fitting the correlation between the position and the momentum, which was calculated by the TOF between two 5-mm-thick plastic scintillators SF1 and SF2. The energy loss up to the hydrogen target was calculated using the code of Ref. [16]. The energy spread on the target was 277–300 MeV/nucleon. The trajectories of the incident beam were tracked with two beam drift chambers (BDCs) placed in front of the target. A bag filled with helium gas at a pressure of 1 atm was inserted between the BDCs to reduce multiple scattering. For ^{9}C, the position and angle resolutions on the target were 130 μm and 0.13 mrad (rms), respectively.

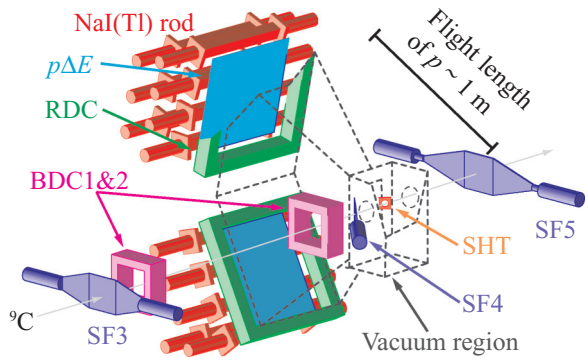

FIG. 2. (Color online) Schematic view of the experimental setup around the SHT.

As the proton target, we use a solid hydrogen target (SHT). The cryogenic system used has been described in detail elsewhere [17]. The system is called a solid hydrogen target for recoil detection in coincidence with inverse kinematics (SH TRICK) [18]. The SHT was 5 mm thick and 35 mm in diameter, and was tilted at an angle of 45°. In order to eliminate background events caused by the beam colliding with a frame of the SHT, a 1-mm-thick plastic scintillator SF4 was placed in front of the target. SF4 had a 30-mm-diameter hole to pass the beam and was tilted at an angle of 45° and placed perpendicular to the SHT. Behind the target, a scintillator SF5 was placed to identify the charge of forward scattered particles. The size of SF5, 160(W) × 160(H) × 10(D) mm^3, covered a sufficient scattering-angle region (>40° in the center-of-mass frame). Since the excited ^{9}C, which has no bound excited states, decays into other nuclides, identifying the charge was very important for selecting the elastic channel, and we were able to use a thick target without concern for the excitation-energy resolution [e.g., 0.4 MeV (rms) for a 1-mm-thick SHT]. In this experiment, the SHT was made of normal H_2. Since the thermal conductivity of solid normal H_2 is not sufficient to withstand the thermal radiation from the surroundings, the central region of the SHT evaporated, creating a hole. Hence, we defined an effective area to be analyzed. The effective area was smaller than the hole of SF4 and included only the clear solid region. The number of protons in the effective volume was estimated to be $3.43(13) \times 10^{22}$ /cm^2 by measuring cross sections for proton scattering from ^{12}C using the ^{12}C primary beam. Events when incident beams passed through areas outside the effective region were eliminated from the analysis with the BDCs. The total number of the ^{9}C beams which hit the effective area was $4.52(9) \times 10^8$ counts. In order to evaluate the background events, we also irradiated the area with $0.389(7) \times 10^8$ of ^{9}C after evaporating the solid H_2 completely.

Two sets of RPS detectors were installed on the upper and lower exit windows of a vacuum chamber which is shown in

Fig. 2 by dashed lines. The flight length of a recoil proton from the SHT to each set was about 1 m. Each set consisted of a recoil drift chamber (RDC), a plastic scintillator ($p\Delta E$), and NaI(Tl) calorimeters. The number of NaI(Tl) rods was seven and five for the upper and lower sides, respectively. The energies of the recoil protons respectively reaching and penetrating the NaI(Tl) rods were about 20 and 120 MeV; these energies corresponded to 80° and 66° of recoil angle, respectively. For the combination of 12 NaI(Tl) rods, the solid angle for every 1° bin of recoil angle became 5–7 msr in the laboratory frame. Because the position resolution in the RDC was less than 0.5 mm (rms) for recoil protons and the energy resolution of the NaI(Tl) rods was 0.3 MeV (rms) for 80 MeV protons [19], the uncertainty of the reaction point in the SHT mainly determined the excitation-energy resolution, which is described later.

The trigger condition of data acquisition consisted of the coincidence of a beam and a recoil particle defined as follows: The beam was defined as a logical AND of signals from SF2 and SF3 and no signal from SF4. For the signal from SF3, we selected $Z = 6$ by roughly discriminating information about energy loss. The recoil particle was defined as a logical OR of signals from $p\Delta E$. The live time as well as all the detection efficiencies were about 90–100%. The errors of the detection efficiencies were $\leqslant 1\%$.

B. Data reduction

Compared with normal kinematics, proton scattering in inverse kinematics is characterized by the kinematical correlation between recoil angle and recoil energy. Figure 3 shows the correlation for recoil protons reaching the upper side of the RPS. We can see a clear locus corresponding to the elastic channel in Fig. 3(a). This results from distinguishing elastically scattered ^{9}C from particles arising from breakup channels with SF5. When we do not use SF5, the clear locus is hidden in the unbound region due to the thick target, as shown in Fig. 3(b). The measurement of the forward scattered particles with SF5, in addition to the missing-mass measurement, has thus greatly facilitated elastic reaction-channel identification for the ^{9}C beam, which is located at the proton drip-line and has no bound excited states below the proton-separation energy.

From the kinematical information of the beam and the recoil proton, the excitation energy of ^{9}C was calculated. Figure 4 shows the excitation-energy spectrum for recoil angles of less than 79°. The solid and dotted lines correspond to the events shown in Figs. 3(a) and 3(b), respectively. We can see a clear peak corresponding to the elastic channel. The excitation-energy resolution was about 1 MeV (rms), as mentioned above. The small gray area in Fig. 4 shows the background events normalized by the number of ^{9}C beams. Due to the pure proton target, the number was extremely small. After subtracting the background events from the peak, we counted the elastic events between ±7.5 MeV for every 1° bin in the laboratory frame.

We obtained the differential cross sections by the following procedure. Since the angular distribution of the measured elastic events is broadened due to the detector resolutions

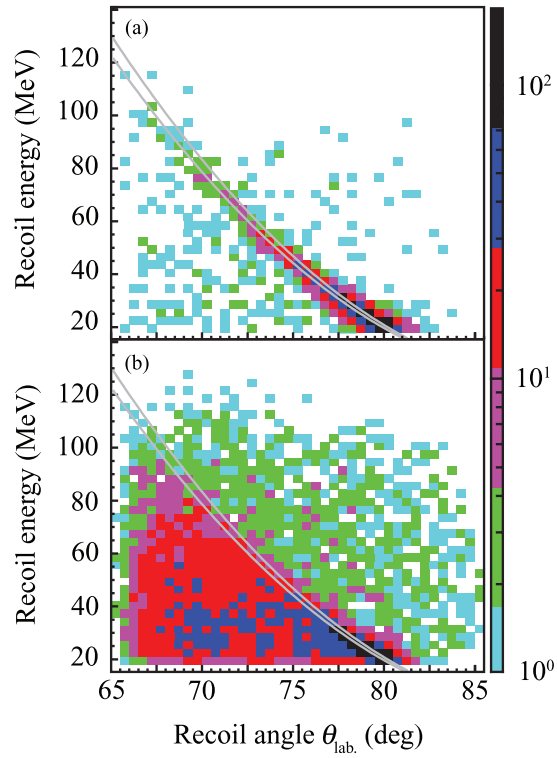

FIG. 3. (Color online) Kinematical correlations between angle and energy for recoil protons. (a) The elastic events and (b) all the events are plotted for the upper side of the RPS. The solid lines indicate the loci of proton elastic scattering at 277 and 300 MeV/nucleon.

mentioned above and the multiple scattering, the present yield $y(\theta_i)$ integrated between $\theta_i \pm \Delta\theta$ of polar angle in the laboratory frame is written as

$$y(\theta_i) = IN \int_{\theta_i-\Delta\theta}^{\theta_i+\Delta\theta} d\theta' \int_0^{\pi} d\sin\theta'' \epsilon(\theta'')\sigma(\theta'') f(\theta' - \theta''), \tag{1a}$$

$$\sigma(\theta) = \int_0^{2\pi} d\psi \left(\frac{d\sigma}{d\Omega}\right)_{\text{lab.}}, \tag{1b}$$

where I, N, and ϵ are the total number of incident beams, the number of target protons, and the detection efficiency. In the above equation, σ is the cross section integrated over the azimuthal angle in the laboratory frame, and f is an instrumental response function. During the numerical procedure, this equation was transformed to a discrete form for every 1° bin ($\Delta\theta = 0.5°$):

$$\begin{pmatrix} y_1 \\ \vdots \\ y_i \\ \vdots \\ y_n \end{pmatrix} = IN \begin{pmatrix} f_{11} & \cdots & f_{1i} & \cdots & f_{1n} \\ \vdots & \ddots & & & \vdots \\ f_{i1} & \cdots & f_{ii} & \cdots & f_{in} \\ \vdots & & & \ddots & \vdots \\ f_{n1} & \cdots & f_{ni} & \cdots & f_{nn} \end{pmatrix} \begin{pmatrix} \epsilon_1\sigma_1 \\ \vdots \\ \epsilon_i\sigma_i \\ \vdots \\ \epsilon_n\sigma_n \end{pmatrix}. \tag{2}$$

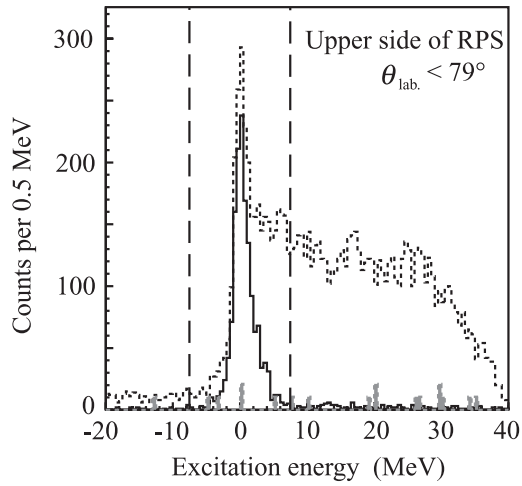

FIG. 4. Excitation-energy spectrum of ^{9}C for recoil angles of less than 79°. The solid line corresponds to the elastic events tagged with SF5. The dotted line corresponds to all the events not tagged. The small gray area is the background events normalized by the number of ^{9}C beams. The dashed lines indicate the gate of ±7.5 MeV for the elastic events.

The matrix elements of the instrumental response function were calculated using the Monte Carlo simulation code GEANT3 [20]. After solving Eq. (2), we obtained the cross sections in the center-of-mass frame by dividing the corresponding solid angle in the center-of-mass frame into σ_i. Lastly, we removed data points around the end of the measured angular region since we do not know the influx of recoil protons from the outside region. The obtained cross sections are plotted in Fig. 5 and are listed in Table V in the Appendix. The experimental error includes statistical and systematic uncertainties in the number of beams, the number of target protons, the number of recoil protons, and the detector efficiencies. Of these, the statistical error of the recoil protons accounted for most of the experimental error. Nuclear reaction loss in the NaI(Tl) [21] was not considered in this analysis because the reduction was much less than the statistical error.

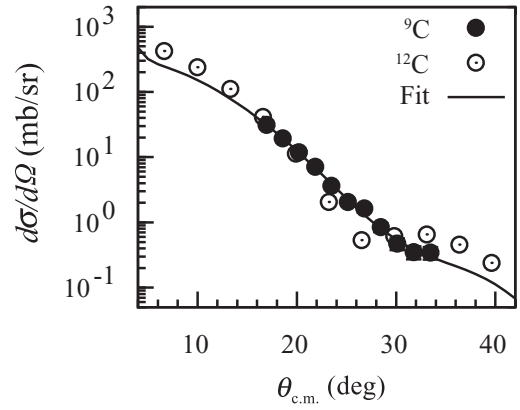

FIG. 5. Angular distribution of the differential cross sections for the H(^{9}C, p) reaction at 277–300 MeV/nucleon (closed circles). The data for ^{12}C are also plotted as a reference (open circles). The best-fit calculation with the modified MH model and the two-parameter Fermi distributions is shown by the solid line.

III. RESULTS AND DISCUSSION

The matter radius of ^{9}C was deduced by fitting the present angular distribution, which shows a smoother diffraction pattern than that of ^{12}C [22] as shown in Fig. 5 (open circles). Section III A describes the reaction model, and the result is given in Sec. III B.

A. Reaction model

We used and modified a model formulated by Murdock and Horowitz (the MH model) [23]. The characteristics of the MH model are that the effective NN scattering amplitude is described by the simple direct plus exchange terms in the framework of the RIA; the pseudovector coupling for the pseudoscalar meson instead of the pseudoscalar coupling restores disagreement with phenomenological optical potentials at low energies. In addition, the MH model can include medium modification from Pauli blocking. However, we applied the medium modification proposed in our previous work [3] to take into account various nuclear many-body effects in terms of the nuclear density. The modification of the effective NN scattering amplitude from the original MH model, which arises in the σ- and ω-meson exchange diagrams, is written as

$$g_i^2, \overline{g}_i^2 \rightarrow \frac{g_i^2}{1 + a_i \rho_{\rm B}(r)/\rho_0}, \quad \frac{\overline{g}_i^2}{1 + \overline{a}_i \rho_{\rm B}(r)/\rho_0}, \tag{3a}$$

$$m_i, \overline{m}_i \rightarrow m_i \left(1 + b_i \frac{\rho_{\rm B}(r)}{\rho_0}\right), \quad \overline{m}_i \left(1 + \overline{b}_i \frac{\rho_{\rm B}(r)}{\rho_0}\right), \quad i = \sigma, \omega, \tag{3b}$$

where g_i^2 are the coupling constants of the nucleon-meson vertexes, m_i are the masses of the propagators, and $\rho_{\rm B}(r)/\rho_0$ is the baryon density divided by the normal density 0.1934 fm^{-3}. An overline indicates an imaginary part.

We determined the phenomenological coefficients a_i, $\overline{a}_i$, b_i, and $\overline{b}_i$ by the same procedure for the medium-heavy stable nuclei [4,5]: the number of coefficients was reduced to four ($a_\sigma = \overline{a}_\sigma$, $b_\sigma = \overline{b}_\sigma$, $a_\omega = \overline{a}_\omega$, $b_\omega = \overline{b}_\omega$), and they were searched by means of the minimum chi-square method. The chi-square is

$$\chi^2 = \sum_{j=1}^{N} \frac{[y_j - y(\theta_j; a_i, b_i)]^2}{\Delta y_j^2}, \tag{4}$$

where N is the number of data points, y_j and Δy_j are the jth experimental data and error, and $y(\theta_j)$ is the calculated cross section at an angle θ_j. In this analysis, we adopted the scattering observables of the ^{12}C($\overrightarrow{p}$, p) reaction at 300 MeV to be fitted because ^{12}C is the nearby stable $N = Z$ nucleus and the charge density distribution was inferred by the electron scattering precisely. Figure 6(a) shows the employed proton vector and scalar density distributions, which are equal to the employed neutron density distributions. The vector density distribution $\rho_{\rm V}(r)$ was extracted by unfolding the sum-of-Gaussians (SOG) charge density distribution [24] with the intrinsic charge distributions of the proton and the neutron [25]. The SOG charge density distribution itself was used for the Coulomb potential. On the other hand, we calculated the scalar

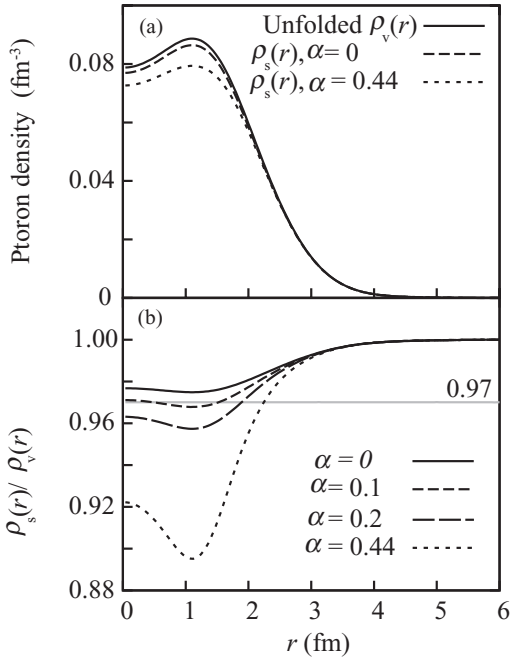

FIG. 6. (a) Unfolded vector density distribution of ^{12}C (solid line). The scalar density distributions for $\alpha = 0$ and $\alpha = 0.44$ are indicated by the dashed and dotted lines, respectively. (b) Ratio of the scalar density to the vector density. The ratios for $\alpha = 0$, 0.1, 0.2, and 0.44 are indicated by the solid, dashed, long-dashed, and dotted lines, respectively. The constant ratio 0.97 is plotted as a guide for the eye as a gray line.

density distribution $\rho_S(r)$ with the approximation described in Ref. [23]:

$$\rho_S(r) = \rho_V(r)\left(1 - \frac{3}{10}\frac{k_F^2}{M^{*2}}\right), \tag{5a}$$

$$k_F^3 = \frac{3}{2}\pi^2\rho_B(r), \tag{5b}$$

$$\frac{M^*}{M} = 1 - \alpha\frac{\rho_B(r)}{\rho_0}, \tag{5c}$$

where k_F is the local Fermi momentum and M is the nucleon mass. The coefficient α is 0.44 in Ref. [23], but we changed the value. Figure 6(b) shows ratios of $\rho_S(r)$ to $\rho_V(r)$ for $\alpha =$ 0, 0.1, 0.2, and 0.44. With a decrease of α, the ratio increases, and the change becomes smooth inside the nucleus. In the relativistic Hartree (RH) calculation [26] for medium-heavy nuclei, the ratio is almost constant and about 0.96 as reported in Refs. [3–5]. For light nuclei, the ratio slightly increases and the ratio in ^{12}C is about 0.97. This characteristic in the RH calculation is compatible with that for $\alpha \sim 0$. Additionally, we examined α by the minimum chi-square method. Figure 7 shows χ^2 for the original and modified MH models as a function of α. χ^2 decreases with a decrease of α, and is almost constant when α is smaller than 0.1. We therefore selected $\alpha = 0$.

The modified MH calculation with the best-fit parameters is shown in Fig. 8 as solid lines. The overestimation of the differential cross sections by the original MH model

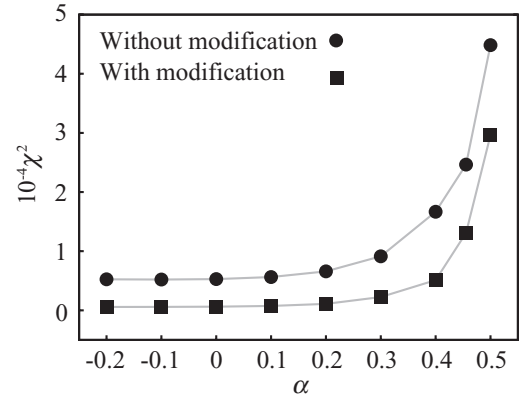

FIG. 7. χ^2s as a function of α. Circles: χ^2 without modification; squares: χ^2 with modification. The lines are guides for the eye.

(dotted line) is improved with $\chi^2 = 493.15$, which is about 10 times smaller than that by the original MH model. The best-fit parameters are listed in Table I. The deviations listed correspond to the maximal and minimal values of each parameter in a joint confidence region which satisfies

$$\chi^2 \leqslant \chi^2_{\min} + \Delta\chi^2, \tag{6}$$

where $\chi^2_{\min}$ is the minimum value of χ^2 and $\Delta\chi^2$ defines the boundary of the present confidence region. In this analysis, $\Delta\chi^2 = 4.72$. This value corresponds to a 68% joint confidence

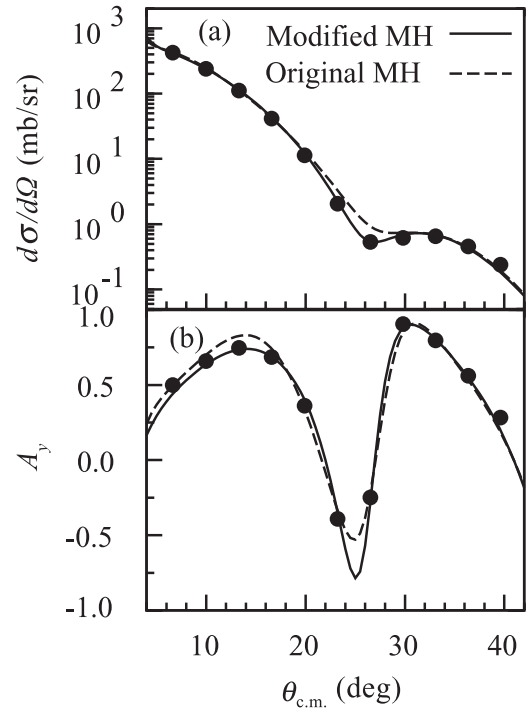

FIG. 8. Comparison of experimental data for the ^{12}C$(\vec{p}, p)$ reaction at 300 MeV with the MH calculations. The data of (a) the differential cross sections and (b) the analyzing powers are taken from Ref. [22]. The solid and dashed curves are the MH calculations with and without modification, respectively.

TABLE I. Coefficients a_i and b_i ($i = \sigma, \omega$) in Eqs. (3).

i	σ	ω
a_i	$-0.391^{+0.016}_{-0.015}$	$-0.529^{+0.027}_{-0.016}$
b_i	$0.356^{+0.013}_{-0.018}$	$0.477^{+0.025}_{-0.037}$

region for four variables whose errors are normally distributed [27].

In the next section, we used the above-mentioned modified MH model and the relation between the vector and scalar densities represented by Eqs. (5) with $\alpha = 0$. The charge density distribution for the Coulomb potential was calculated by folding the vector density distributions with the intrinsic charge distributions of the proton and the neutron [25].

B. Matter radius of ^{9}C

The present angular distribution was fitted with two-parameter Fermi distributions for protons and neutrons:

$$\rho_i(r) = \frac{N_i}{1 + \exp\{(r - R_i)/a_i\}}, \quad i = p, n, \tag{7}$$

where N_i are the normalization coefficients and R_i and a_i are free parameters. Using the density distributions, we obtained the rms matter radius $\langle r_m^2 \rangle^{1/2}$ as

$$\langle r_m^2 \rangle = \frac{1}{A} \int d\boldsymbol{r}\, \rho_p(r) r^2 + \frac{1}{A} \int d\boldsymbol{r}\, \rho_n(r) r^2, \tag{8}$$

where A is the target mass number.

The best-fit calculation is presented in Fig. 5 as a solid line. The fit reproduces the data qualitatively well. Table II lists the deduced rms matter radius, the best-fit χ^2, and the geometry parameters. The present rms matter radius is consistent with the radii deduced from the measurements of the interaction cross sections [6] and the reaction cross sections [28] within the errors (Table III). The value also agrees with the experimental radii of ^{9}Li deduced from the measurement of the elastic scattering of protons at 700 MeV/nucleon [9] as well as the measurements of the interaction cross sections [6] and the reaction cross sections [29].

We evaluated the error of the rms matter radius in a similar manner to the phenomenological coefficients in Eqs. (3) since the rms matter radius was determined by the four free parameters R_i and a_i through Eq. (8). Figure 9 shows the confidence region for the parameter set (R_i, a_i). Note that the minimum χ^2 was found using the remaining two free parameters for every fixed parameter set (R_p, a_p) or (R_n, a_n). The confidence regions which satisfy Eq. (6) are roughly enclosed by solid and dashed curves. The solid and dashed curves in Fig. 9(a) correspond to the solid and dashed curves in Fig. 9(b), respectively. The parameter sets in the solid and dashed curves yield proton and neutron skins, respectively. From the parameter sets in the regions, we obtained the maximal and minimal rms matter radii, and adopted them as the errors of the rms matter radius.

In Fig. 9, we can roughly see valleys from the upper left to the lower right of the figure in both the proton and neutron sides and can thereby find out the confidence region splitting into two parts. The emergence of the two valleys implies that it is appropriate to deduce the radius rather than the density distribution because the radius is not sensitive to the correlation between R_i and a_i, as the proton and neutron rms radii are

TABLE II. Deduced rms matter radius (fm), best-fit χ^2, and geometry parameters (fm).

$\langle r_m^2 \rangle^{1/2}$	χ^2	R_p	R_n	a_p	a_n
$2.43^{+0.55}_{-0.28}$	5.15	3.345	1.647	0.307	0.070

TABLE III. Experimental matter radii (fm) of ^{9}C and ^{9}Li. The values deduced from the measurements of the proton elastic scattering, the interaction cross sections σ_I, and the reaction cross sections σ_R are listed.

	(p, p)	σ_I	σ_R
^{9}C	$2.43^{+0.55}_{-0.28}$[a]	2.42(3)[b]	2.75(34), 2.71(32)[c]
^{9}Li	2.44(6)[d]	2.32(2)[b]	2.534(25)[e]

[a]This work.
[b]Reference [6].
[c]Reference [28].
[d]Reference [9].
[e]Reference [29].

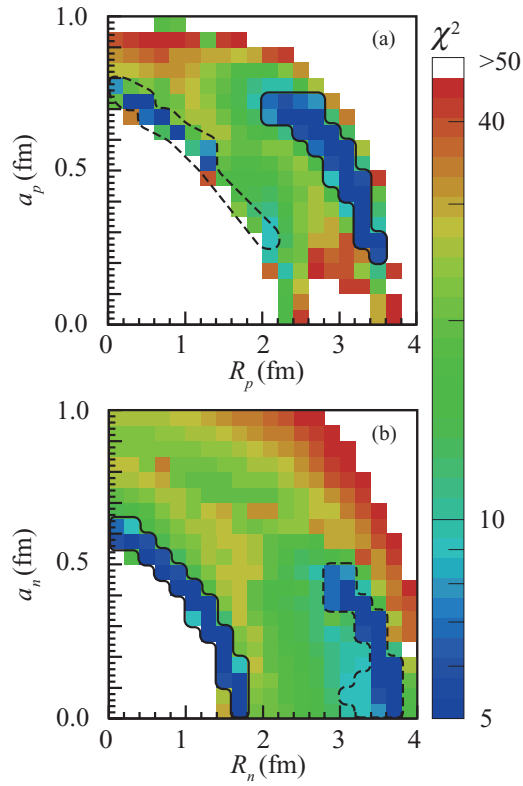

FIG. 9. (Color online) Two-dimensional confidence regions for the parameter sets (a) (R_p, a_p) and (b) (R_n, a_n). The regions which satisfy Eq. (6) are enclosed by the solid and dashed curves.

TABLE IV. Root-mean-square matter radii (fm) of ^{9}C with the RH and MAMD calculations.

	This work	RH	MAMD
$\langle r_m^2 \rangle^{1/2}$	$2.43^{+0.55}_{-0.28}$	2.58	2.40[a]

[a]Reference [31].

approximately written as

$$\langle r_i^2 \rangle \sim \tfrac{3}{5} R_i^2 + \tfrac{7}{5} \pi^2 a_i^2, \quad (9)$$

using the Sommerfeld expansion [30]. The splitting of the confidence region indicates that it is inappropriate to use the same geometry parameters for protons and neutrons even though we use large diffuseness parameters so as to reflect the smooth diffraction pattern. Instead of them, the present diffraction pattern was reproduced well by spreading out one distribution while the other distribution remained inside the nucleus. Because the rms matter radius is approximately represented by such a quadratic sum of four geometry parameters, a proton or neutron skin appeared in this analysis. Unfortunately, the splitting of the confidence region also indicates that the present data are not sensitive to the proton and neutron density distributions independently. Hence, in order to determine the skin thickness, we need to measure another experimental observable which has different sensitivity to the proton and neutron density distributions than the present observable.

Finally, we compare the present result with two theoretical densities based on the RH and multiple-width Gaussian basis antisymmetrized molecular dynamics (MAMD) [31]. Table IV shows the RH and MAMD matter radii. These sizes agree with the present rms matter radius within the errors. Concerning angular distribution, the calculations with the RH and MAMD densities reproduce the present data with $\chi^2 \simeq 30$ and 40, respectively (Fig. 10). The calculations also have a similar behavior to the present fit in the measured momentum transfer region. However, the present fit overestimates both calculations at forward and backward angles. Hence, additional data on cross sections at these angles are necessary to discuss the details of the density distribution.

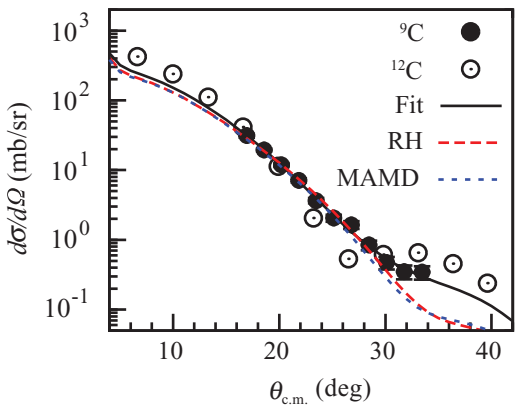

FIG. 10. (Color online) Comparison of the experimental data with calculations using theoretical densities. The dashed and dotted lines show the calculations with the RH [26] and MAMD [31] densities, respectively. The other notations are the same as those in Fig. 5.

IV. SUMMARY

We have developed a recoil proton spectrometer to measure the elastic scattering of protons with radioactive ion beams. Using the spectrometer, cross sections for proton elastic scattering from ^{9}C at 277–300 MeV/nucleon were measured. The matter radius was deduced with the relativistic folding model formulated by Murdock and Horowitz. In this analysis, the reaction model was modified to reproduce the cross sections and the analyzing powers for proton elastic scattering from ^{12}C at 300 MeV. The proton and neutron density distributions were assumed to be two-parameter Fermi distributions.

The root-mean-square matter radius was deduced to be $2.43^{+0.55}_{-0.28}$ fm. This value is consistent with the radii deduced from the measurements of the interaction cross sections and the reaction cross sections. It also agrees with the experimental radii of the mirror nucleus ^{9}Li.

ACKNOWLEDGMENTS

The authors express their gratitude to Dr. Takeshi Murakami, Dr. Eiichi Takada, and the staff of the Accelerator Engineering Corporation at the HIMAC for their assistance with this experiment. This work was supported by the Grant-in-Aid for Young Scientists B(23740164) from the Japan Society for the Promotion of Science (JSPS), and the Grant-in-Aid for the Global COE Programs "Weaving Science Web beyond Particle-Matter Hierarchy" and "The Next Generation of Physics, Spun from Universality and Emergence" from the Ministry of Education, Culture, Sports, Science and Technology (MEXT) of Japan. This work was performed as one of Research Projects with Heavy Ions at NIRS-HIMAC.

APPENDIX: NUMERICAL DATA TABLE

TABLE V. Differential cross sections of the H(^{9}C, p) reaction at a beam energy of 277–300 MeV. The angle integrated $\pm 0.5^\circ$ in the laboratory frame corresponds to $\pm\Delta\theta_{c.m.}$ in the center-of-mass frame. The error $\pm\Delta(d\sigma/d\Omega)_{c.m.}$ includes statistical and systematical uncertainties (for details see the text).

$\theta_{c.m.}$ (deg)	$\pm\Delta\theta_{c.m.}$	$\left(\frac{d\sigma}{d\Omega}\right)_{c.m.}$ (mb/sr)	$\pm\Delta\left(\frac{d\sigma}{d\Omega}\right)_{c.m.}$
16.948	0.813	31.3	2.1
18.576	0.815	19.4	1.0
20.209	0.817	11.86	0.80
21.846	0.820	7.14	0.51
23.488	0.822	3.66	0.33
25.134	0.825	2.05	0.23
26.787	0.827	1.64	0.21
28.444	0.830	0.84	0.13
30.108	0.834	0.472	0.098
31.779	0.837	0.351	0.080
33.456	0.840	0.343	0.076

[1] T. Kobayashi, O. Yamakawa, K. Omata, K. Sugimoto, T. Shimoda, N. Takahashi, and I. Tanihata, Phys. Rev. Lett. **60**, 2599 (1988).
[2] I. Tanihata, J. Phys. G: Nucl. Part. Phys. **22**, 157 (1996).
[3] H. Sakaguchi *et al.*, Phys. Rev. C **57**, 1749 (1998).
[4] S. Terashima *et al.*, Phys. Rev. C **77**, 024317 (2008).
[5] J. Zenihiro *et al.*, Phys. Rev. C **82**, 044611 (2010).
[6] A. Ozawa, T. Suzuki, and I. Tanihata, Nucl. Phys. A **693**, 32 (2001).
[7] R. Sánchez *et al.*, Phys. Rev. Lett. **96**, 033002 (2006).
[8] O. A. Kiselev *et al.*, Eur. Phys. J. A **25**, 215 (2005).
[9] A. V. Dobrovolsky *et al.*, Nucl. Phys. A **766**, 1 (2006).
[10] S. Ilieva *et al.*, Nucl. Phys. A **875**, 8 (2012).
[11] K. Matsuta *et al.*, Nucl. Phys. A **588**, c153 (1995); Hyperfine Interact. **97/98**, 519 (1996).
[12] M. Huhta *et al.*, Phys. Rev. C **57**, R2790 (1998).
[13] Y. Utsuno, Phys. Rev. C **70**, 011303 (2004).
[14] M. Kanazawa *et al.*, Nucl. Phys. A **746**, 393 (2004).
[15] Y. Matsuda, T. Kobayashi, M. Itoh, K. Ozeki, H. Sakaguchi, J. Zenihiro, Y. Iwao, H. Otsu, H. Takeda, and S. Terashima, Nucl. Instrum. Methods Phys. Res. A **670**, 25 (2012).
[16] M. H. Salamon, Berkley LBL Report 10446 (1980).
[17] Y. Matsuda *et al.*, Nucl. Instrum. Methods Phys. Res. A **643**, 6 (2011).
[18] A. Obertelli and T. Uesaka, Eur. Phys. J. A **47**, 105 (2011).
[19] J. Zenihiro *et al.*, CYRIC Annual Report, 2005, p. 20; Y. Matsuda *et al.*, CYRIC Annual Report, 2006, p. 15.
[20] GEANT *3.2.1*, CERN Computing Library (1993).
[21] C. A. Goulding and J. G. Rogers, Nucl. Instrum. Methods **153**, 511 (1978).
[22] A. Tamii *et al.*, Nucl. Instrum. Methods Phys. Res. A **605**, 326 (2009).
[23] D. P. Murdock and C. J. Horowitz, Phys. Rev. C **35**, 1442 (1987); C. J. Horowitz, D. P. Murdock, and B. D. Serot, in *Computational Nuclear Physics 1*, edited by K. Langanke, J. A. Maruhn, and S. E. Koonin (Springer-Verlag, Berlin, 1991), Chap. 7.
[24] H. de Vries, C. W. de Jager, and C. de Vries, At. Data Nucl. Data Tables **36**, 495 (1987).
[25] W. M. Alberico, S. M. Bilenky, C. Giunti, and K. M. Graczyk, Phys. Rev. C **79**, 065204 (2009).
[26] C. J. Horowitz and B. D. Serot, Nucl. Phys. A **368**, 503 (1981).
[27] P. R. Bevington and D. K. Robinson, *Data Reduction and Error Analysis for the Physical Sciences*, 3rd ed. (McGraw-Hill, New York, 2003).
[28] R. E. Warner *et al.*, Phys. Rev. C **74**, 014605 (2006).
[29] E. Liatard *et al.*, Europhys. Lett. **13**, 401 (1990).
[30] A. Sommerfeld, Z. Phys. **47**, 1 (1928); N. W. Ashcroft and N. D. Mermin, *Solid State Physics* (Thomson Learning, New York, 1976).
[31] N. Furutachi, M. Kimura, A. Doté, and Y. Kanada-En'yo, Prog. Theor. Phys. **122**, 865 (2009).